Metrologia

The uncertainty of counting at a defined solid angle

To cite this article: S Pommé 2015 *Metrologia* **52** S73

OPEN ACCESS
IOP Publishing | Bureau International des Poids et Mesures Metrologia
Metrologia **52** (2015) S73–S85 doi:10.1088/0026-1394/52/3/S73

The uncertainty of counting at a defined solid angle

S Pommé

European Commission, Joint Research Centre, Institute for Reference Materials and Measurements, Retieseweg 111, B-2440 Geel, Belgium

E-mail: stefaan.pomme@ec.europa.eu

Received 2 September 2014, revised 7 November 2014
Accepted for publication 11 November 2014
Published 22 May 2015

Abstract

Specific uncertainty components of counting at a defined solid angle are discussed. It is potentially an extremely accurate technique for primary standardisation of activity of alpha emitters and low-energy x-ray emitters. Owing to its reproducibility, it is very well suited for half-life measurements. Considered sources of uncertainty are 1) source–detector geometry, 2) solid-angle calculation, 3) energy loss and self-absorption, 4) scattering, 5) detection efficiency. Other sources of uncertainty, such as source weighing, counting, dead time and decay data are common to other standardisation methods. Statistical uncertainty propagation formulas are presented for the solid angle subtended by a circular detector to radioactive sources. Computer simulations were performed to investigate aspects of particle scattering.

Keywords: uncertainty, alpha, x ray, primary standardisation, radioactivity, solid angle

(Some figures may appear in colour only in the online journal)

1. Introduction

Counting at a defined solid angle (DSA) is, together with coincidence counting, a valuable alternative to high-geometry methods for primary standardisation of activity [1]. High-geometry methods generally aim at counting all radiation emitted by a radioactive source, in any emission angle. The source material may be integrated in the sensitive part of the detector, as is the case with liquid scintillation counting [2] and internal gas counting [3], but generally it is dispensed on a very thin backing [4] and surrounded by the detector in a 4π counting geometry [1]. These methods typically require a correction for the non-detected fraction of the decays. If the non-efficiency is due to particle or photon absorption in the source and backing material at low emission angles, it may be advantageous to restrict counting to a well-defined, small fraction of radiation emitted perpendicular to the source plane. Energy loss and self-absorption are comparably low for this fraction, such that the detection efficiency nearly equals the geometrical efficiency. The observed count rate must be corrected by the geometry factor, $\Omega/4\pi$, which involves accurate distance measurements and mathematical modelling of the subtended solid angle.

In a 'defined solid angle' method (see e.g. [1, 5–7] and references therein), only the part of the radiation that is emitted into the solid angle subtended by the detector or by the aperture of the diaphragm covering it, is measured. The method assumes isotropic emission of one or a precisely known (average) number of particles per decay, which move undisturbed along a straight line and are counted when they hit the detector directly. The particles emitted in other directions should not be counted, but rather be absorbed in the diaphragm or other materials, without scattering into the detector or transmission through the diaphragm edge. These conditions can be met by alpha particles of several MeV and low-energy photons in the range 1 keV to 20 keV, but not by the easily scattering β particles [5, 6].

In a low-geometry counter, the geometrical efficiency is not higher than a few per cent of 4π, whereas geometries covering higher solid angles (but lower than 50% of 4π) are called medium-geometry counters. Set-ups for alpha-particle counting at a defined solid angle have been described in literature

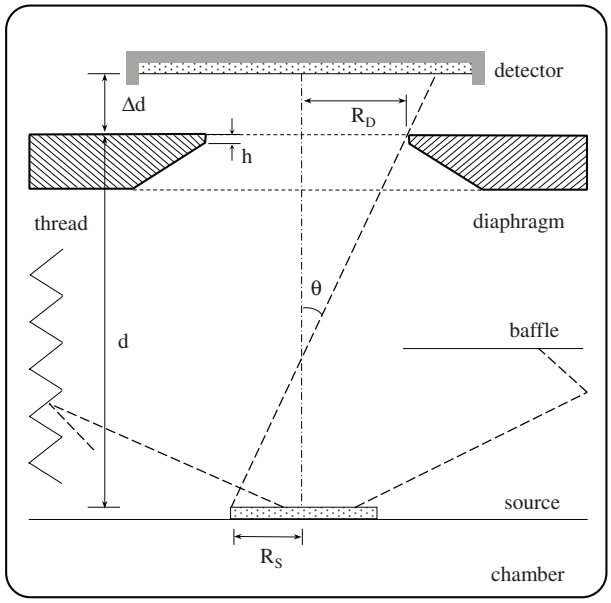

Figure 1. Schematic representation of characteristic geometrical parameters.

by several institutes, including IRMM (formerly CBNM) [8, 9], LRL [10], NIST [11], ANL [12], CIEMAT [13, 14], LNE-LNHB [15, 16] and PTB [17]. New set-ups have recently been constructed in TAEK (Turkey) and NPL (UK), inspired by the IRMM model. Specifically for the standardisation of activity concentration of ^{222}Rn gas, defined solid angle counters were built in which the gas could be condensed on a cold plate and measured in a ion-implanted planar silicon detector under vacuum conditions [18–20].

The uncertainty components involved with low-geometry alpha counting have been discussed in the past [5, 6, 16]. It was concluded that uncertainties as low as 0.02% should be feasible. An intercomparison of activity measurements with defined low solid angle set-ups in two institutes has indeed revealed agreement of alpha-particle emission rates of six ^{233}U sources within 0.01%–0.05% [8], whereas 0.1% uncertainty was estimated on the activity. In recent work, authors report improvements in the characterisation of the geometrical efficiency to an estimated accuracy of 0.007% [21]. In this work, the main uncertainty components are investigated.

2. Source-detector geometry

Excellent control of the geometrical conditions of the setup is an essential requirement to reach a state-of-the-art level of accuracy. This comprises different aspects, e.g. the careful design and mechanical construction of different set-up parts, the accurate determination of distances for the evaluation of the solid angle subtended by the detector, the use of a detector with known detection efficiency and the production of thin and uniform sources on a flat substrate.

In figure 1 some essential geometrical elements are shown in a schematic representation of a typical DSA set-up, including source, support, diaphragm, detector, baffle and chamber. The symbols represent the diaphragm radius R_D, the source radius R_S, the distance d between source and upper diaphragm plane, the distance Δd between diaphragm and detector window, the diaphragm edge thickness h, and the emission angle θ.

2.1. Chamber and spacers

As measurements are performed in vacuum, the source and detector are enclosed in a vacuum chamber, most often of cylindrical geometry. The source is mounted on a source holder at the bottom of the set-up, facing up to the window and the sensitive layer of the detector mounted on top of the chamber. Extracting the gas molecules is done to minimize absorption and scattering of photons or particles on their way from source to detector. However, scattering is also possible against the inner chamber walls and a fraction of the scattered particles may end up on the sensitive detector area. Measures need to be taken to avoid a non-negligible fraction of particles emitted at wide angles being counted in this manner (see section 4). The radius of the cylindrical tube can be increased, which reduces the effective solid angle of the detector for particles scattering off the wall [5, 16]. A very effective measure is the installation of baffles [5, 6], which are thin metallic plates with a central aperture placed in parallel with the source and detector plane, to stop particles flying towards or scattered away from the side wall (see figure 1). Another effective idea is to give the side walls of the cylindrical spacer a sharp, knife-edge thread, thus reducing the effective surface and reflecting sputtered contamination towards the lower side of the thread helix [21].

Important aspects of a chamber are stability and reproducibility of the geometrical conditions. For the calculation of the solid angle, the simplicity of cylindrical symmetry is an advantage. Therefore, source and diaphragm are centred around the symmetry axis and care is taken that both are flat and their planes are parallel. Most set-ups have a fixed geometry or have a segmented construction that allows for a discrete number of geometrical configurations. The recent set-up in CIEMAT [14] is an exception in that it allows the source mount to vary continuously in the vertical direction; the position of the sample holder with respect to the detector diaphragm is measured with an optical linear encoder with absolute reference marks to retrieve its absolute position if that reference is lost.

One of the crucial geometrical parameters is the distance between source and detector, which is not usually measured directly but determined as a sum of distances of various components. In a very simple design used e.g. at PTB [17], the source and diaphragm planes are connected by metal distance rods. This distance can be determined in an SI-tracable manner by comparing it with a stack of gauge blocks of similar height, using a height gauge with digital or dial readout. IRMM uses a segmented design with source chamber, distance tube and diaphragm fitting together on smoothly connecting flanges. The distance between diaphragm and a reference plate in the source holder can be measured directly or calculated from the sum of the heights of the individual components with an accuracy of about (5–20) μm. The distance seems unaffected by vacuum pumping. At NIST, the uncertainty on the

source-to-detector distance was estimated at 1.6 μm only using a microscope system which had to be corrected for a bias of 3.3 μm observed with gauge blocks simulating the same distance. The distance uncertainty of about 60 μm is significantly larger in the moveable CIEMAT configuration.

All distances are measured at a fixed temperature and thermal equilibrium should be re-established after manual handling. Temperature variations in the laboratory during DSA measurements lead to thermal expansion in the chamber material. The thermal expansion coefficient for copper (and stainless steel) is 16.6 $10^{-6}\,K^{-1}$, which means that a tube of 100 mm expands by 8.3 μm with a 5 K temperature rise. At the same time, the diameter of the diaphragm increases proportionally, which cancels out the effect on the solid angle. This is demonstrated mathematically in section 3 and practical proof was found in an ^{225}Ac half-life measurement with 20 K temperature variation showing stability within about 0.1% [22].

2.2. Detector

For alpha-particle measurements, large ion-implanted silicon detectors (up to 5000 mm^2) with an ultra-thin window (< 50 nm) and 100% intrinsic detection efficiency are commonly used. The sensitive detector area is flat and circular, fitted into a metal housing with a collar. To avoid difficulties with accurate determination of its radius and possible fringe effects, a circular diaphragm is placed in front of the detector, thus masking the outer part of the detector and constraining the subtended solid angle.

There are potentially a few processes that may diminish the actual detection efficiency: (1) the detector radius being too small to cover the theoretical solid angle derived from the aperture of the diaphragm; (2) dust particles on the detector blocking a fraction of the incoming particles; (3) a non-zero probability for particles being scattered back in the dead layer of the detector.

In practice the detector is placed above the diaphragm (figure 1), with a spacing Δd between its window surface and the diaphragm top. Therefore, the detector radius should not be smaller than the diaphragm radius R_D increased with an amount $\Delta d(R_S + R_D)/d$. This amount is needed to measure the particles entering at the most extreme angle. Whereas the detector surface is theoretically assumed to be pristine, this has to be checked visually and adhering dust particles should be removed (e.g. by blowing it off with compressed air). A total covered area of 1 mm^2 on a surface of 1000 mm^2 can constitute a significant source of error in a precise measurement. Backscattering of alpha particles in silicon is estimated below 0.01% [5]. The probability for backscattering is much larger for electrons (ca. 10–30%), which implies big correction factors [23] and disqualifies the DSA method for primary standardisation of the activity of beta emitters.

For the measurement of x photons, a gas-filled proportional counter with a thin entrance window is an option [24]. Low-Z construction materials that create fluorescence x-rays should be avoided. The transmission probability through the detector window has to be calculated and combined with the interaction probability inside the gas volume (and averaged over the impact angle). For example, at IRMM a measurement of ^{55}Fe activity in a P10-filled gas counter with 25 mm Be window was performed with 95% detection efficiency, the transmission part being 98.9%. The associated uncertainty was estimated around 2%.

2.3. Diaphragm

The measurement geometry can be much better controlled with the introduction of a circular diaphragm, not only by its sharper defined aperture radius R_D but also due to the possibility to firmly position it in a parallel plane to the source support at a well-defined distance d. With the same detector, solid angles can be varied by applying different diaphragm apertures. The inner radius can be measured with great accuracy. At IRMM, a standard uncertainty of 5 μm was assigned to diameters (hence half this amount to the radii) of (20–60) mm measured with an ABBE comparator and later confirmed with a Mitutoyo digital microscope.

More detailed investigations were performed at NIST, using three instruments: a Nikon MM-400SL measuring microscope, a Mitutoyo UMAP 100 coordinate measuring machine (CMM) and a laser device. The latter was not ideally suited for this purpose and disagreed by 2 μm with the other methods. The first two methods, with estimated standard uncertainties of 0.5 μm and 0.24 μm, agreed within 0.8 μm [21].

Diaphragms are constructed with a sloping edge to avoid particle scatter onto the detector (figure 1). Nevertheless, they are not produced razor sharp at the inside since a minimum thickness h is needed to stop the radiation. At IRMM, typical values for h are (0.1–0.2) mm of stainless steel. Measurement of the physical diameter of the aperture needs to be complemented with calculations of the transmission probability of particles or photons through the edge [5, 21, 25–27], which depends on energy (range of particles, attenuation coefficient of photons), angle of impact and energy threshold. In the particular case of 5,157 keV ^{239}Pu alpha particles impinging with an average angle of 8.38 degrees and a copper/nickel throat of 0.5 mm, NIST researchers calculated an 1.8 (6) μm increase of the effective diameter due to aperture edge penetration [21].

2.4. Source

Conventionally, sources are placed on top of a holder and the thickness of the substrate as well as the activity distribution in the active layer need to be accounted for to optimize the precision of the effective solid angle. A thickness measurement can be avoided in a configuration in which the source is pressed upwards against a source holder with central recess, so that the active material of a flat source is always at the level of the bottom plane of the source holder (PTB).

The so-called Robinson chamber, which has a medium geometry factor of nearly 1π sr, has been made less sensitive to vertical and horizontal displacement of the source by adding a central conical stop in front of the detector. Mathematical equations were presented to optimize the choice of distance and radius of a circular stop for a point source and a more

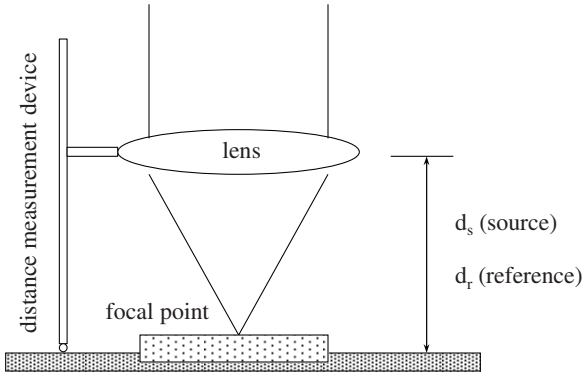

Figure 2. Schematic representation of source height measurements using an optical focussing technique.

general solution for a combination of stops to make the chamber also less sensitive to non-uniformity in the activity distribution of a large-area source [10, 11].

A contemporary solution consists of assessing the radioactivity distribution through autoradiography and determining the vertical position of the active layer by an optical method, since contact with the radioactive material needs to be avoided. In section 3, it is discussed how the accuracy of the method can be greatly improved by taking the geometrical distribution of the radioactive material in the source into account in the solid-angle calculation. As shown schematically in figure 2, a travelling lens connected to a distance-measuring device can be used to determine the difference in height between the source and a reference plate in the source holder, by optically focussing on their surfaces. It is good practice to repeat the measurement in different points of the active source area, as thickness differences of (10–20) μm are frequently observed due to inhomogeneity or focussing problems. Focussing is also impeded by transparency of glass, quartz or thin film substrates, by deep surface scratches or by superficial dust particles. Only in optimal conditions of source homogeneity and thickness (< 4 μm) can unusually low uncertainty estimates in the order of 1 μm [21] be considered.

3. Solid-angle calculation

Whereas the solid-angle calculation was initially performed on the basis of approximate formulae or Monte Carlo simulations (see e.g. [1, 28–32]), there are nowadays exact mathematical analytical solutions for commonly used geometries [33–50]. The most common configuration involves a coaxial circular diaphragm and a quasi-circular source. Uncertainty propagation on the distance d and radius R_D will be investigated first through the simple equation for a point source. Then exact equations for a circular source are used to propagate the uncertainty on R_S. As drop-deposited sources are neither perfectly round nor homogenous, a method is investigated that uses an autoradiograph of the source to adjust the solid angle according to the location of the activity. Also the consequences of imperfect circularity of the diaphragm, thickness of the aperture edge and a slight tilt between the source and diaphragm planes are calculated.

3.1. Point source

An idealised situation is that of a source with negligible dimensions—a 'point' source—positioned on the symmetry axis of a perfect diaphragm-detector combination that allows for 100% detection efficiency for particles travelling directly through the aperture and zero transmission at wider angles. The exact analytical expression for the subtended solid angle is

$$\Omega_P = 2\pi(1-\cos\theta) = 2\pi\left(1-\frac{1}{\sqrt{1+R_D^2/d^2}}\right) \quad (1)$$

in which θ is the maximum value of the emission angle leading to detection:

$$\theta = \arctan\left(\frac{R_D}{d}\right) \quad (2)$$

The uncertainty on the solid angle Ω_P follows then from the propagation of the uncertainty on the polar angle:

$$\sigma(\Omega_P) = \left|\frac{d\Omega_P}{d\theta}\right| \sigma(\theta) = 2\pi\, sin\theta\, \sigma(\theta) \quad (3)$$

The corresponding relative uncertainty is:

$$\frac{\sigma(\Omega_P)}{\Omega_P} = \left[\frac{\theta\sin\theta}{1-\cos\theta}\right]\frac{\sigma(\theta)}{\theta} \approx \left[2-\frac{\theta^2}{6}-\frac{\theta^4}{360}-\ldots\right]\frac{\sigma(\theta)}{\theta} \quad (4)$$

By approximation for small angles ($R_D < d$), the relative uncertainty on the solid angle is twice that of the polar angle.

The uncertainty on the polar angle will generally be calculated from the relative uncertainties on the distance d and the radius R_D. Independent variations in one of these geometrical variables propagate to Ω_P via:

$$\sigma(\Omega_P) = \left|\frac{\partial\Omega_P}{\partial R_D}\right|\sigma(R_D) = 2\pi\left(1+\frac{R_D^2}{d^2}\right)^{-3/2}\frac{R_D}{d^2}\sigma(R_D) = 2\pi(\cos\theta)^3(\tan\theta)^2\frac{\sigma(R_D)}{R_D} \quad (5)$$

and

$$\sigma(\Omega_P) = \left|\frac{\partial\Omega_P}{\partial d}\right|\sigma(d) = \left|-2\pi\left(1+\frac{R_D^2}{d^2}\right)^{-3/2}\frac{R_D^2}{d^3}\right|\sigma(d) = 2\pi(\cos\theta)^3(\tan\theta)^2\frac{\sigma(d)}{d} \quad (6)$$

The corresponding relative uncertainties are:

$$\frac{\sigma(\Omega_P)}{\Omega_P} = \left[\frac{(\cos\theta)^3}{1-\cos\theta}(\tan\theta)^2\right]\frac{\sigma(R_D)}{R_D} \approx \left[2-\frac{3}{2}\theta^2+\frac{3}{8}\theta^4-\ldots\right]\frac{\sigma(R_D)}{R_D} \quad (7)$$

and

$$\frac{\sigma(\Omega_P)}{\Omega_P} = -\left[\frac{(\cos\theta)^3}{1-\cos\theta}(\tan\theta)^2\right]\frac{\sigma(d)}{d} \approx -\left[2-\frac{3}{2}\theta^2+\frac{3}{8}\theta^4-\ldots\right]\frac{\sigma(d)}{d} \quad (8)$$

By rough approximation for small angles ($R_D << d$), the relative uncertainty on the solid angle is almost twice that of the distance and radius. An uncertainty of $\sigma(R_D)$ =2 μm on a radius of R_D = 20 mm ($\sigma(R_D)/R_D$ = 0.01%) corresponds to $\sigma(\Omega_P)/\Omega_P$ = 0.02% uncertainty on the solid angle for d > 100 mm, but significantly less at smaller distances, e.g. $\sigma(\Omega_P)/\Omega_P$ = 0.006% at d = 10 mm. An uncertainty of 5 μm on a distance d = 50 mm ($\sigma(d)/d$ = 0.01%) corresponds to $\sigma(\Omega_P)/\Omega_P$ = 0.02% uncertainty for a small diaphragm of R_D < 20 mm, but less for large diaphragms, e.g. $\sigma(\Omega_P)/\Omega_P$ = 0.003% for R_D = 200 mm.

Certain errors or variations in d and R_D may be correlated, such as a common measurement error or simultaneous changes through thermal expansion. The uncertainty caused by correlated changes (with correlation factor ρ) in the dimensions involves a third term:

$$\sigma^2(\Omega_P) = \left[\frac{\partial\Omega_P}{\partial R_D}\right]^2\sigma^2(R_D) + \left[\frac{\partial\Omega_P}{\partial d}\right]^2\sigma^2(d) + 2\rho\left(\frac{\partial\Omega_P}{\partial R_D}\right)\left(\frac{\partial\Omega_P}{\partial d}\right)\sigma(R_D)\,\sigma(d) \quad (9)$$

and, by introducing equations (7)–(8), the combined relative uncertainty is:

$$\frac{\sigma(\Omega_P)}{\Omega_P} = \left[\frac{(\cos\theta)^3}{1-\cos\theta}(\tan\theta)^2\right] \times\left[\left(\frac{\sigma(R_D)}{R_D}\right)^2+\left(\frac{\sigma(d)}{d}\right)^2-2\rho\frac{\sigma(R_D)}{R_D}\frac{\sigma(d)}{d}\right]^{1/2} \quad (10)$$

Positively correlated changes of the dimensions due to variations in temperature tend to cancel out. If the diaphragm and distance tube have the same coefficient of expansion, then the correlation factor is one, hence the corresponding uncertainty increase is zero.

3.2. Eccentric point source and centred ring source

The solid angle subtended by a circular detector with radius R_D for a non-coaxial point source at a distance a from the symmetry axis can be calculated exactly from [41]:

$$\Omega_P = 4\pi\frac{R_D}{2}\int_0^\infty J_0(sa)\,J_1(sR_D)\;e^{-sd}\,ds \quad (11)$$

in which $J_0(x)$ and $J_1(x)$ are Bessel functions of the first kind. Due to the cylindrical symmetry, the same equation is also directly applicable to a centred ring-shaped source with radius $R_S = a$. The equation can be evaluated using a mathematical software package or pre-defined functions in a spreadsheet. Alternatively, one can apply a solution based on numerical integration [40] or a series expansion of equation (11) [45, 46] which converges well for $d > a + R_D$, i.e. at relatively high source–detector distances:

$$\Omega_P \approx 4\pi\left[\frac{R_D}{2d}\right]^2\sum_{l=0}^{\infty}\sum_{m=0}^{\infty}\left(-\frac{1}{4}\right)^{l+m}\left(\frac{R_D}{d}\right)^{2l}\left(\frac{a}{d}\right)^{2m}\frac{[2(l+m)+1]!}{l!\,(l+1)!\,m!^2} \quad (12)$$

One can also use approximating formulas [12, 29] (which are fairly accurate for $a < R_D$) to estimate the uncertainty propagation due to a displacement a of a source from its theoretical position:

$$\frac{\Omega_P(a)-\Omega_P(0)}{\Omega_P(0)} \approx \frac{-\frac{3}{8}\frac{a^2R_Dd}{D^5}+\frac{15}{32}\frac{a^4R_D^2d}{D^9}\left(d^2-\frac{3}{4}R_D^2\right)}{\frac{1}{2}\left(1-\frac{d}{D}\right)} \quad (13)$$

in which D is defined as $\sqrt{d^2+R_D^2}$. Uncertainty of $\sigma(a)$ = 1 mm on the horizontal displacement of the source in a configuration with d = 50 mm and R_D = 20 mm leads to $\sigma(\Omega_P)/\Omega_P$ = 0.05% uncertainty on the solid angle around the centre a = 0 mm, but much higher uncertainties where the gradient of the solid angle is higher: e.g. $\sigma(\Omega_P)/\Omega_P$ = 1.7% near a = 20 mm.

Figure 3 shows Ω_P as a function of a in four configurations: R_D/d = 10/1, 5/2, 1/1 and 1/10. For a very small diaphragm (or at high distance) the solid angle is low, but its gradient is relatively small. At very close distance to the diaphragm (or very large diaphragm), the solid angle is high for $a < R_D$, but the slope is steep as the solid angle becomes very low at acute angles.

3.3. Homogenous disk source

The source is represented by a flat disk with a radius R_S, characterised by a homogeneous distribution of the active material and an isotropic emission of the particles. The circular detector diaphragm with radius R_D is positioned in a plane parallel with the source plane. The orthogonal distance between both planes equals d and a possible eccentric positioning of the source is characterised by the distance a between the symmetry axes of source and detector.

Before exact solutions were available, approximating equations were used. For small sources, there are relatively simple approximations by Jaffey *et al* [12, 29]:

$$\Omega_S \approx 4\pi\left(\frac{1}{2}\left(1-\frac{d}{D}\right)-\frac{3}{16}\frac{a^2R_Dd}{D^5}+\frac{5}{32}\frac{a^4R_D^2d}{D^9}\left(d^2-\frac{3}{4}R_D^2\right)\right) \quad (14)$$

and others, e.g. Segré [30] and Blachman [28], the applicability of which is usually restricted to small, centred sources at sufficient distance from the detector [32, 42].

An exact solution for the solid angle subtended by a circular detector to a parallel circular source has been provided by Ruby and Rechen [34, 38] and generalised by Conway [43]:

$$\Omega_S = 4\pi\frac{R_D}{R_S}\int_0^\infty\frac{J_0(sa)J_1(sR_D)J_1(sR_S)}{s}\,e^{-sd}\,ds \quad (15)$$

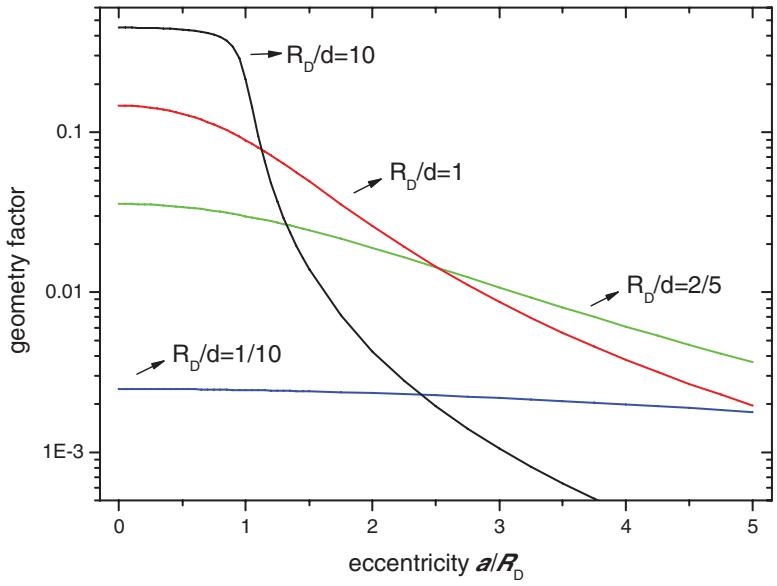

Figure 3. Relative solid angle subtended by a disk shaped detector with radius R_D to a point source at four distances d to the detector and as a function of the radial distance a of the source to the symmetry axis of the detector.

Again, a numerical integration method [40] can provide the exact solution. Equation (15) includes the solution for an eccentric source, translated by a distance a from the detector symmetry axis. It can also be expressed as a serial expansion [45] which works well for $d > a + R_S + R_D$:

$$\Omega_S \approx \pi \sum_{k=0}^{\infty}\sum_{l=0}^{\infty}\sum_{m=0}^{\infty}\left(-\frac{1}{4}\right)^{k+l+m}\left(\frac{a}{d}\right)^{2k}\left(\frac{R_D}{d}\right)^{2l+2}\left(\frac{R_S}{d}\right)^{2m} \times \frac{[2(k+l+m)+1]\,!}{k\,!^2\, l\,!\,(l+1)\,!\,m\,!\,(m+1)\,!} \quad (16)$$

For smaller source–detector distances, the series involves the summation of huge terms with opposite sign and does not easily converge to realistic values. Sensitivity factors can be easily obtained from differentiation of equation (16). For example, defining $G(k, l, m)$ as the term in the summations, independent variations of the eccentricity a leads to the following uncertainty contribution to Ω_S:

$$\frac{\sigma(\Omega_S)}{\Omega_S} = \left|\frac{\partial\Omega_S}{\partial a}\right| \frac{a}{\Omega_S}\frac{\sigma(a)}{a} \approx \frac{\pi}{\Omega_S}\left|\sum_{k=0}^{\infty}\sum_{l=0}^{\infty}\sum_{m=0}^{\infty} G(k,l,m)\,2k\right|\frac{\sigma(a)}{a} \quad (17)$$

Similar sensitivity factors as those in equation (17) are easily obtained for R_S, R_D and d, replacing the factor $2k$ by $2m$, $(2l + 2)$ and $-2(k + l + m + 1)$ respectively.

Just as for a point source, the uncertainty due to a small horizontal shift of the source is low for a small centred source, but increases by orders of magnitude for large off-centre sources for which the solid angle varies significantly in various points of its surface. For R_S = 10 mm and d = 50 mm, a shift by Δa = 1 mm changes Ω_S by 0.04%, 0.9% and 1.6% at a = 0 mm, 10 mm and 20 mm respectively.

Conway presented a quickly converging integral representation of the solid angle for coaxial disks [43]. It can be transformed into the following form [45]:

$$\Omega_S = 2\frac{R_D}{R_S}\int_0^{\pi}\frac{\sin^2\Phi}{\sqrt{x-\cos\Phi}\left(\sqrt{y}+\sqrt{x-\cos\Phi}\right)}\,d\Phi \quad (18)$$

in which x and y are defined as $x = R_S^2 + R_D^2 + d^2 / 2R_SR_D$ and $y = d^2 / 2R_SR_D$.

The integral representation (equation (18)) can be implemented in software as a sum:

$$\Omega_S = \frac{2\pi}{n}\frac{R_D}{R_S}\sum_{i=1}^{n}\frac{\sin^2\varphi}{\sqrt{x-\cos\varphi}\left(\sqrt{y}+\sqrt{x-\cos\varphi}\right)} \quad (19)$$

in which $\varphi = (i - 0.5)\pi/n$ and n is an integer value of choice (e.g. $n = 50$). This is a quickly converging solution that reaches a high accuracy already for modest values of n. It is the best choice among the available formulas, provided that the source is centred on the symmetry axis of the detector.

The following partial derivatives can be used for the uncertainty propagation:

$$\frac{\partial}{\partial x}\frac{\sin^2\varphi}{\sqrt{x-\cos\varphi}\left(\sqrt{y}+\sqrt{x-\cos\varphi}\right)} = \frac{-\sin^2\varphi\left(\sqrt{y}+2\sqrt{x-\cos\varphi}\right)}{2\left(\sqrt{x-\cos\varphi}\right)^3\left(\sqrt{y}+\sqrt{x-\cos\varphi}\right)^2}$$

$$\frac{\partial}{\partial y}\frac{\sin^2\varphi}{\sqrt{x-\cos\varphi}\left(\sqrt{y}+\sqrt{x-\cos\varphi}\right)} = \frac{-\sin^2\varphi}{2\sqrt{y}\sqrt{x-\cos\varphi}\left(\sqrt{y}+\sqrt{x-\cos\varphi}\right)^2}$$

$$R_S\frac{\partial x}{\partial R_S} = \frac{R_S^2 - R_D^2 - d^2}{2R_SR_D} \qquad R_S\frac{\partial y}{\partial R_S} = \frac{-d^2}{2R_SR_D}$$

$$R_D\frac{\partial x}{\partial R_D}=\frac{R_D^2-R_S^2-d^2}{2R_DR_S} \qquad R_D\frac{\partial y}{\partial R_D}=\frac{-d^2}{2R_SR_D}$$

$$d\frac{\partial x}{\partial d}=\frac{d^2}{R_DR_S} \qquad d\frac{\partial y}{\partial d}=\frac{d^2}{R_DR_S}$$

Defining the function $\mathrm{T}(n)=\dfrac{\sin^2\varphi}{\sqrt{x-\cos\varphi}\left(\sqrt{y}+\sqrt{x-\cos\varphi}\right)}$, the relative uncertainty on the solid angle due to the uncertainty on the source radius R_S is

$$\frac{\sigma(\Omega_S)}{\Omega_S}=\frac{\sigma(R_S)}{R_S}\frac{R_S}{\Omega_S}\frac{2\pi}{n}\left|\sum_{i=1}^{n}\frac{\partial}{\partial R_S}\left[\frac{R_D}{R_S}T(n)\right]\right|$$
$$=\frac{\sigma(R_S)}{R_S}\frac{1}{\Omega_S}\frac{2\pi}{n}\frac{R_D}{R_S}\left|\sum_{i=1}^{n}-T(n)+\frac{\partial \mathrm{T}(n)}{\partial x}\frac{\partial x}{\partial R_S}R_S+\frac{\partial T(n)}{\partial y}\frac{\partial y}{\partial R_S}R_S\right| \quad (20)$$

due to the diaphragm radius:

$$\frac{\sigma(\Omega_S)}{\Omega_S}=\frac{\sigma(R_D)}{R_D}\frac{R_D}{\Omega_S}\frac{2\pi}{n}\left|\sum_{i=1}^{n}\frac{\partial}{\partial R_D}\left[\frac{R_D}{R_S}T(n)\right]\right|$$
$$=\frac{\sigma(R_D)}{R_D}\frac{1}{\Omega_S}\frac{2\pi}{n}\frac{R_D}{R_S}\left|\sum_{i=1}^{n}T(n)+\frac{\partial \mathrm{T}(n)}{\partial x}\frac{\partial x}{\partial R_D}R_D+\frac{\partial \mathrm{T}(n)}{\partial y}\frac{\partial y}{\partial R_D}R_D\right| \quad (21)$$

due to the source–diaphragm distance:

$$\frac{\sigma(\Omega_S)}{\Omega_S}=\frac{\sigma(d)}{d}\frac{d}{\Omega_S}\frac{2\pi}{n}\left|\sum_{i=1}^{n}\frac{\partial}{\partial d}\left[\frac{R_D}{R_S}T(n)\right]\right|$$
$$=\frac{\sigma(d)}{d}\frac{1}{\Omega_S}\frac{2\pi}{n}\frac{R_D}{R_S}\left|\sum_{i=1}^{n}\frac{\partial T(n)}{\partial x}\frac{\partial x}{\partial d}d+\frac{\partial T(n)}{\partial y}\frac{\partial y}{\partial d}d\right| \quad (22)$$

A numerical problem may arise when values are close to zero (e.g. $a\to 0$ or $R_S\to 0$, while their uncertainty is not ($\sigma(a)>a$, $\sigma(R_S)>R_S=>\ \sigma(a)/a\to\infty$, $\sigma(R_S)/R_S\to\infty$). In order to obtain a realistic uncertainty also in the cases where $a<\sigma(a)/2$, $R_S<\sigma(R_S)/2$, one can apply in the uncertainty formulas a fictitious value of $a=\sigma(a)/2$ and $R_S=\sigma(R_S)/2$.

3.4. Telescope and thick diaphragm

As the inner edge of a diaphragm is given a thickness h to avoid transmission of particles, the top and bottom side of the aperture correspond to a different solid angle. Particles emitted from a central position ($a<R_D$) in the source see the top side of the aperture as the defining edge, while particles emitted from very eccentric positions ($a>R_D$) are partly stopped due to interaction with the bottom side of the aperture. Ignoring in the first instance transmission and deflection effects, a thick aperture is geometrically equivalent with a telescope of two coaxial diaphragms. There is no closed mathematical equation for a set-up with two diaphragms. A solution for multiple diaphragms has been implemented in numerical integration routines by Pommé *et al* [40] and can in principle also be dealt with by simulation.

The integration of the solid angle can be split up into two parts, $\Omega=\Omega_1+\Omega_2$, depending on the eccentricity r of the considered point in the source:

$$\Omega_1=\begin{cases}2\pi(1-\cos\theta') & for\ r<R_D\\ 0 & for\ r\geq R_D\end{cases} \quad (23)$$

in which $\theta'=\arctan\left((R_D-r)/d\right)$ corresponds to the most extreme polar angle in which the azimuthal angle φ can be integrated over 2π, whereas in the second part the boundary angles must be calculated:

$$\Omega_2=\int_{\theta_1}^{\theta_2}2\left(\pi-\varphi(\theta)\right)\sin\theta\,\mathrm{d}\theta \quad (24)$$

in which $\theta_1=\arctan\left(\left|\dfrac{R_D-r}{d}\right|\right)$, $\theta_2=\arctan\left(\dfrac{R_D+r}{d}\right)$,

and $\varphi(\theta)=\arccos\left(\dfrac{R_D^2-\{r^2+d^2\tan^2\theta\}}{2r\,d\,\tan\theta}\right)$.

The first term (equation (23)) is zero if $r>R_D$, whereas the second term (equation (24)) is zero if $r=0$, i.e. for a point on the symmetry axis.

The following procedure provides the correct solid angle for a set-up with two coaxial, circular diaphragms, possibly having different dimensions. First, for each eccentricity value r, the lower and upper limits of the angle θ are determined for both diaphragms:

$$\theta_1^{(i)}=\arctan\left(\frac{r-R_{D_i}}{d_i}\right)\ \text{and}\ \theta_2^{(j)}=\arctan\left(\frac{r-R_{D_j}}{d_j}\right) \quad (25)$$

in which the indexes i and j refer to the diaphragm ($i,j=1$ or 2). The limiting angles are determined from:

$$\theta_1=\max\left\{\theta_1^{(i)}\right\}\ \text{and}\ \theta_2=\min\left\{\theta_2^{(j)}\right\} \quad (26)$$

If the values θ_1 and θ_2 refer to the same diaphragm, equation (24) can be applied directly. If they refer to a different diaphragm, one has to calculate the polar angle θ_3 at which to switch the integration from one diaphragm to another, i.e. the angle θ at which the integration over the angle φ is equal for both diaphragms:

$$\theta_3=\arctan\left(\sqrt{\frac{R_{D_1}^2-r^2}{d_1(d_1-d_2)}-\frac{R_{D_2}^2-r^2}{d_2(d_1-d_2)}}\right) \quad (27)$$

A similar procedure is applied for a triple set of coaxial diaphragms: if the values θ_1 and θ_2 refer to a different diaphragm, the role of the third diaphragm is investigated. If the azimuthal angle obtained at θ_3 is more restrictive than for the other diaphragms, i.e. $2(\pi-\varphi(\theta_3)^{(3)})<2(\pi-\varphi(\theta_3)^{(1,2)})$, the corresponding transition angle has to be calculated and the integration is performed in three intervals [40]. In a set of four coaxial

diaphragms, at least one of the four will not play a role in the effective solid angle.

3.5. Elliptical diaphragm

The assumption of perfect roundness may not always rigorously apply to real diaphragms, i.e. the aperture radius may show local deviations ΔR_D from the mean value R_D. The real shape of the aperture may, for example, be elliptical with semi-axes $a = R_D + \Delta R_D$ and $b = R_D - \Delta R_D$. Then the question arises as to the size of the error on the calculated solid angle when nevertheless applying the equation for a circular detector with radius R_D. Conway [47, 48] has published an exact solution for the solid angle subtended by an elliptical detector with semi-axes a and b to a disk source. An adapted version is shown below:

$$\Omega_{\text{ellips}} = 4\pi \frac{1}{R_S} \int_0^{\infty} \frac{J_1(sR_S)}{s} e^{-sd} \left[R_D J_1(sR_D)\, J_0(s\Delta R_D) - \Delta R_D J_1(s\Delta R_D)\, J_0(sR_D) \right] \mathrm{d}s \tag{28}$$

in which a and b have been substituted by the average radius $R_D = (a + b)/2$ and the boundary value for deviations from roundness $\Delta R_D = (a - b)/2$. From numerical tests, it was concluded that the solid angle for a coaxial elliptic detector to a disk source, $\Omega_{\text{ellips}}(a, b, R_S, d)$, is well approximated by the equation (15) for a circular aperture with average radius R_D, $\Omega_{\text{circle}}(R_D, R_S, d)$. The relative error on the thus obtained solid angle is by approximation equal to:

$$\frac{\Omega_{\text{circle}}(R_D, R_S, d)}{\Omega_{\text{ellips}}(R_D, \Delta R_D, R_S, d)} - 1 \approx \left(\frac{\Delta R_D}{R_D} \right)^2 \tag{29}$$

Consequently, one can reduce the error of this approximation by at least an order of magnitude, by subtracting this component:

$$\Omega_{\text{ellips}}(R_S, R_D, \Delta R_D, d) \approx \Omega_{\text{circle}}(R_D, R_S, d) \left[1 - \left(\frac{\Delta R_D}{R_D} \right)^2 \right] \tag{30}$$

Ten per cent deviation on the roundness of the detector—$\Delta R_D/R_D = 0.1$—leads to only one per cent difference in the solid angle: $\Omega_{\text{circle}}/\Omega_{\text{ellips}}\text{-}1 = 0.01$. Application of the simple correction rule to Ω_{circle} in equation (30), reduces the error to only 0.025%. For very small $\Delta R_D/R_D$ (< 0.03), even better results are obtained by correcting with the ratio $\Delta R_D/b$.

3.6. Tilted source or diaphragm

The constant value of the source–diaphragm distance implies that both planes are perfectly flat and in parallel. If for some practical reason this is not the case in reality, one could apply generalised solid-angle formulas for a rotated disk detector [47] or use the following approach: for a diaphragm being tilted by a small angle x upwards at one side, the projection of the effective surface of the aperture in the plane corresponding to the shortest source–diaphragm distance d to a centred point source takes the shape of an ellipse with long axis R_D and short axis $R_D \cos(x)$. Equations (28) or (30) can be applied to calculate the corresponding solid angle.

3.7. Eccentric, inhomogeneous sources

Quantitative sources prepared by drop deposition [4] of an active solution on a substrate are to some extent inhomogeneous and out-of-centre [41]. Even sources prepared by a more advanced technique like e.g. vacuum evaporation [4] may deviate from the ideal disk shape. The effective solid angle for a source is an average value for each particle that is emitted and therefore a weighted mean should be taken accounting for the activity distribution within the active layer. In principle, the source area can be subdivided into small pixels for which the solid angle can be calculated in the central point and the relative weight of the pixel should correspond to the fraction of the activity residing in that position. The latter can be assessed by digital [41] or scanned photo film [14] autoradiography.

Owing to the axial symmetry of the set-up, it is more convenient to subdivide the source into a mesh of thin, concentric, annular regions of interest centred on the symmetry axis. Thin rings unite all points situated at a similar radial distance and therefore corresponding to a nearly identical solid angle. A simple integration of the activity inside the ring suffices as a weighting factor, irrespective of how the activity is distributed in the azimuthal degree of freedom.

The solid angle of a ring-shaped homogeneous source having its symmetry axis in common with the circular diaphragm can be calculated by integration of the point solid angle at displacements r varying between the inner and outer radius of the ring, R_{in} and R_{out}:

$$\Omega_R = \frac{\int_{R_{in}}^{R_{out}} \Omega_P\, 2\pi r\, \mathrm{d}r}{\pi (R_{out}^2 - R_{in}^2)} \tag{31}$$

A convenient alternative is to derive the solid angle of the ring source from a combination of the solid angles for two disk sources with radius R_{in} and R_{out}, using the fast and accurate algorithm in equation (19) and the following relationship [9]:

$$\Omega_R = \frac{R_{out}^2 \Omega_S(R_{out}) - R_{in}^2 \Omega_S(R_{in})}{R_{out}^2 - R_{in}^2} \tag{32}$$

The introduction of autoradiography has greatly improved the accuracy and speed of the method. In the past, measurements of a source were performed at different (high) distances and the activity was derived from an extrapolation of the apparent activity values towards zero solid angle. Equation (13) can be used to simulate the residual error due to an unknown radial displacement a, when extrapolating results taken at two distances d_1 and d_2. Disregarding a source displacement of $a/R_D = 1/2$ at distances $d_1/R_D = 1$ and $d_2/R_D = 2$ leads to errors of 11% and 6% respectively and a residual 3% after linear extrapolation (assuming zero statistical uncertainty). See also figure 2 in [41] for the extrapolation result due to an error in the radius of a disk source.

3.8. Limitations of autoradiography

When taking an autoradiograph of a radioactive source, a small distance is maintained between the active material and the film surface to avoid activity loss and contamination. As a result of the angular freedom and the discrete travel distance and deposition range, the image of the deposited alpha particles in the film is somewhat diffused around the projected (x, y) position of origin. The film has to be erased first (e.g. by exposure to bright white light) and the remaining background noise level subtracted from the recorded intensities. The exposure to the source has to be sufficiently long to acquire statistical accuracy, however without reaching saturation in the most active areas. Measures have to be taken to identify the geometrical centre of the source on the autoradiograph, on which the concentric regions of interest can be focussed. This can be done by fitting the source in a predefined recess in a source holder together with point sources in three corners which act as references for the coordinate system in the digital photo.

Random uncertainties may arise from poor statistical accuracy in the autoradiograph, possible inhomogeneity in the sensitivity of the film and errors in establishing the source centre due to ill-defined coordinates and some play of the source in the recess. These components can be investigated by repeatedly assessing the radial activity distribution of a source in different conditions. Resolution broadening is considered a systematic error, which repeatedly projects a point as a spot, its wideness depending on the distance between source and film and on the range of the particle across the film surface. This can be verified experimentally by taking autoradiographs at various distances between source and film. From the theoretical side, the radial distribution can be smeared out mathematically and its effect on the solid angle studied. To some extent, the diffusion effect can be countered by inverting the diffusion matrix.

At IRMM, repeatability tests have been performed on radiography of > 30 mm-diameter ^{238}U drop deposited sources of about 10 Bq and the subsequent solid-angle calculation for compact geometries of G = (5.6–6.5)%. Due to the random components mentioned above, the calculated solid angle varied by about 0.1%, which is significant. Moreover, autoradiographs were taken at various distances between source and film to investigate the effect of increasing blur of the image. The calculated solid angles slowly decreased due to the broadening of the radial distribution compared to the reference position at 0.15 mm spacing, by about –0.02 (5)% at 0.30 mm, –0.08 (4)% at 0.45 mm, –0.08 (4)% at 0.6 mm, –0.32 (4)% at 1.03 mm and –0.80 (6)% at 2.18 mm.

4. Interference, scattering and absorption

4.1. Interference

The defined solid angle method relies on the condition that all radiation emitted within the solid angle Ω subtended by the diaphragm aperture is counted and all other radiation is not. The background level in a silicon detector is generally very low ($<10^{-3}$ s^{-1}) and the energy of alpha particles is high (> 4 MeV), which should ultimately lead to a signal that is well separated from noise and radiation from photons and even beta particles. The signal-to-noise ratio is less favourable for x-rays counted in a gas proportional counter.

Contamination of the detector and chamber by recoiled α emitters can be avoided by covering the source with a thin polymer foil. Possible impurities in the enriched material can be identified with high-resolution α-particle or γ–ray spectrometry. Corrections for in-growth must be applied if any of the daughter nuclides emits α particles and in particular if they cannot be distinguished from the parent decay.

Statistical uncertainties are easy to handle, since the square root of the number of counted events is a good estimator of the standard deviation of the Poisson process. In cases where a long-lived parent is in equilibrium with short-lived alpha-emitting daughter nuclides, the statistical uncertainty has to be increased for the multiple events following one parent decay, as these events are correlated. The usual measures and uncertainties related to dead time and pile-up have to be taken into account, even though these effects may be lower than in high-geometry methods.

In figure 4 a spectrum is shown of a very active ^{222}Rn source measured at LNE-LNHB. It reveals interference from the alpha-emitting ^{218,214}Po progeny and also sum peaks produced by random pile-up of combinations of these signals, representing 0.3% of the activity. The insert of figure 4 shows the pile-up spectrum of a source with ‘normal’ activity level in which the pile-up fraction is lower (0.1%) and the sum peaks are clearly distinguishable. The double ^{222}Rn pile-up peak represents two decays per event and therefore should be counted double to compensate for count loss.

4.2. Energy loss and absorption

Additional compensation for count loss below the electronic threshold can be made by extrapolation of the low-energy spectrum towards zero energy. Crucial to the magnitude of this uncertainty component are the processes that determine the size of the low-energy tailing of the alpha peaks. The main contributor is energy loss of the particles in the source material and other energy absorbing layers on their way to the sensitive part of the detector. This is a significant uncertainty component if e.g. half of the extrapolated fraction is adopted as uncertainty value, hence the need for small grain size and preferably a homogenous distribution of the active material to keep the extrapolated fraction below (0.1–0.2)%. If the extrapolated fraction rises above ca. 0.5%, additional corrections have to be made for count loss through total absorption (which is equivalent to an invisible peak at zero energy). These situations are characterised by a negative correlation between source mass and activity concentration results.

4.3. Scattering

Tailing of alpha peaks can also be caused by scattering of particles that were not emitted within the intended solid angle. The emission angles from backscattering in the source backing are generally too low to produce a significant amount of detectable events if 2π configurations are avoided [51, 52].

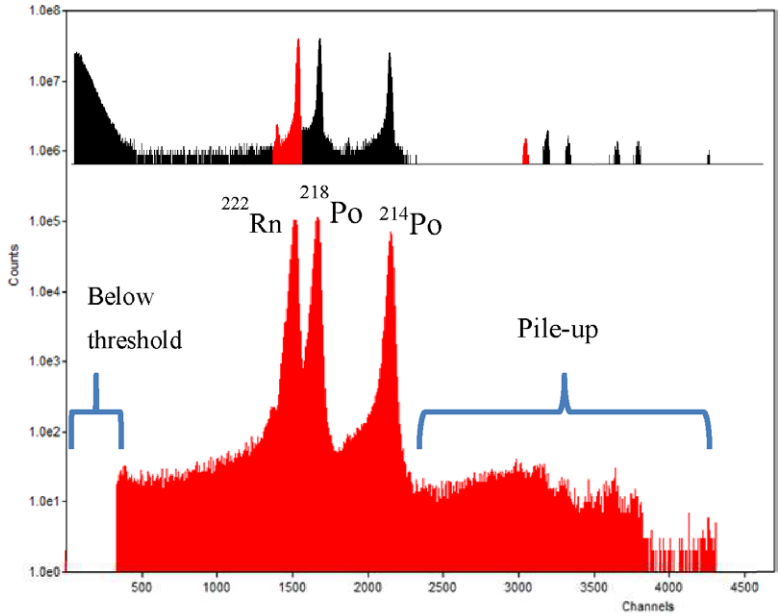

Figure 4. Alpha spectrum of ^{222}Rn taken in a defined solid angle counter for noble gases, using a cold finger on which to condensate the gas. Bottom: spectrum from a highly active source with a considerable pile-up fraction. Top: better resolved spectrum from a 160 kBq source, showing individual sum peaks.

Reflection of particles from the side wall into the detector is more likely to occur. The corresponding probabilities have been investigated in the past through theoretical calculations and experimental tests using inner tubes of various diameters [5, 6, 16]. Also interaction with gas particles has been considered [5, 53] and studied at different gas pressure, but should be insignificant in vacuum. The reader is referred to these papers for detailed equations and conclusions.

In unfavourable conditions, the scattered fraction could amount to 10^{-3}, in particular inside long and narrow tubes and for low-energy alphas [16]. This can be reduced by the introduction of a baffle at half distance, which is even more effective against the low-energy signals of electrons or beta particles and facilitates the extrapolation to zero energy [6]. Scattering on a collimator internal edge of $h = 0.12$ mm contributed typically by a fraction of 10^{-5} particles [16].

At LNE-LNHB, new simulations were performed with MCNPX to compare the scattering probability with the calculations made by Blanchis [16] for a geometry comprised of a disk shaped source and 300 μm-thick silicon detector ($R_S = 8$ mm, $R_D = 10$ mm, $d = 590$ mm) and a 150 mm-radius stainless steel wall of 590 mm height. In total, the trajectories of 55 10^9 alpha particles of 5.48556 MeV were simulated and a fraction of 3.9 (2) 10^{-3} was counted after scatter against the wall, which is much higher than the value of 1.3 10^{-3} published by Blanchis [16].

Figure 5 shows the residual energy distribution of the alpha particles scattered into the detector, which varies between 0 and 2.2 MeV and no noticeable contribution between 2.5 MeV and 5.4 MeV. Setting an energy threshold at (1–2) MeV removes most of the scattered particles, but also cuts off degraded particles. Scattered particles should be excluded from interpolations, while degraded particles should be included. This distinction may be difficult to make around 1 MeV, which adds to the uncertainty of the method.

4.4. Transmission of the diaphragm

Photons and particles not completely absorbed or reflected by the diaphragm edge may contribute to the spectrum of counted events. Low-energy photons passing through the edge, contrary to the particles, suffer no energy loss and contribute to the full detection peak. Particles penetrating the diaphragm edge will suffer energy loss and be part of the tailing fraction. Their contribution should either be taken into account by a correction factor, as is the case for photons or excluded by setting a sufficiently high energy threshold. Simulating or calculating the transmission factor for photons and the energy loss of particles in the diaphragm material requires an integration over all source points and emission angles, since the effective thickness of the edge varies radially and with the angle of incidence.

The range of a 5 MeV alpha particle in iron (density = 7.847 g cm^{-3}) is 10 μm [54]. A thickness of $h = 100$ μm should therefore amply suffice to stop particles that impact the diaphragm edge orthogonally. However, if the aperture diameter is large, the particles can impinge on the inner edge by an angle θ and possibly traverse it sidewise at the top rim. By approximation, the range of an alpha particle can be represented as a power function of its energy [55]. Given the initial energy E_0 (e.g. 5 MeV) of the alpha particle and the threshold energy E_x (e.g. 1 MeV), the event will be counted if the traversed amount of material is less than:

$$T \approx a\left(E_0^b - E_x^b\right) \tag{33}$$

in which $a \approx 1.09$ and $b \approx 1.37$ for iron, expressing E in MeV and T in micron. For $E_0 = 5$ MeV and $E_x = 1$ MeV, the alpha

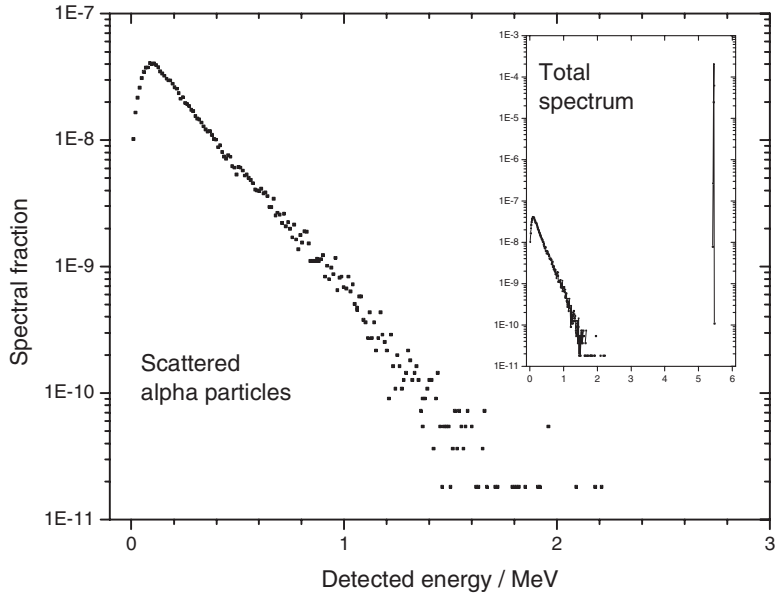

Figure 5. Simulated spectrum showing directly counted alpha particles and a scattered fraction reflected from the inner wall of the chamber (see text).

particles can traverse up to $T = 8\,\mu$m of iron. This increases the effective radius of the diaphragm by an amount $\Delta R_D = T\sin\theta$. For a centred point source at $d = 5$ cm and radius $R_D = 2$ cm, the aperture radius increases by $\Delta R_D = 3\,\mu$m. For a copper diaphragm ($a \approx 1.53$, $b \approx 1.21$), $E_0 = 5.157$ MeV, $E_x = 2.5$ MeV and average angle $<\theta> = 0.146$, the radius increases by $\Delta R_D = 0.8\,\mu$m, comparable to the case in [21].

5. Uncertainty budget

In table 1 an overview of typical uncertainty components is shown with relative uncertainty values for a hypothetical measurement of a 5 MeV alpha and 5 keV x-ray emitting source. The numbers are rough estimates and very much dependent on the specific set-up, source and measurement conditions. They can be compared with estimates made by other authors [5, 21].

Many of the main uncertainty components, e.g. geometry, activity distribution, scattering and transmission, affect the detection efficiency, which complicates the absolute activity measurement of a source. Other uncertainty components can be reduced by repetition, such as counting statistics, background subtraction and weighing drop deposited sources from a stock solution to determine its activity concentration. When performing repeated measurements of one source, e.g. for a half-life measurement, most of these uncertainty components can be omitted, except for counting statistics, pile-up and dead-time correction and possible variations in source repositioning and impurity contributions.

Table 1. Typical uncertainty components of a fictitious activity measurement by defined solid angle counting.

	α (5 MeV)	X (5 keV)
	u (%)	u (%)
source–diaphragm distance d	0.05	0.05
source eccentricity	0.01	0.01
activity distribution	0.05	0.05
broadening autoradiograph	0.004	0.007
aperture radius R_D	0.03	0.03
transmission diaphragm edge	0.02	0.02
transmission detector window	<0.01	0.5
detection efficiency + dust	0.01	0.8
backscattering from source + support	0.01	0.03
scattering at chamber wall	0.01	0.03
extrapolation to zero energy	0.05	0.1
background	<0.01	0.05
counting statistics	0.01	0.01
pile-up and dead time	0.02	0.02
SUM	0.1	1

6. Conclusions

Counting at a defined solid angle is potentially the most accurate method for activity measurements of alpha emitters and is also well suited for x-ray emitters. Accuracy and reproducibility are best achieved in a fixed or modular design. Axial symmetry is most commonly used for ease of modelling. Thermal expansion has little effect on the counting efficiency. Distance measurements have become more precise. Exact mathematical equations are available to perform solid-angle calculations for common geometries. Autoradiography has improved the performance of the method. Interfering events from particles scattered from the source or chamber wall can be reduced actively. Transmission through the detector window and diaphragm edge can be calculated. Peak tailing is an indicator of energy degradation (up to total absorption), scattering and transmission. Thin, homogenous sources on flat substrates and low solid angles generate lower tailing. Detector surfaces need to be cleared of dust particles and must cover the full solid angle subtended by the diaphragm.

Radioactive solutions can be standardised with 0.1% for alpha emitters and 1% for x-ray emitters, including the uncertainty from weighing of the dispensed amounts in the sources. The activity of each specific source can be measured with better accuracy. The repeatability of the activity measurement of a source can be achieved within 0.01%, depending also on counting statistics. The technique is extremely well suited for half-life measurements, either by specific activity measurement of long-lived nuclides or decay curve analysis of intermediately long-lived nuclides, provided that dead-time compensation and interfering signals are well under control. Statistical uncertainty can be a dominant factor, depending on source activity and measurement time.

Acknowledgments

The author gratefully acknowledges the contributions of several colleagues to various parts of this paper. Explicit thanks are due to Sylvie Pierre, Benoit Sabot, Jean Gouriou and Cheick Thiam of LNE-LNHB for performing simulations of the particle scattering in a cylindrical chamber; Maria Marouli for performing a repeatability study of solid-angle calculations with autoradiography and David Gilliam (NIST), Eduardo Garcia-Torano (CIEMAT), Arzu Arinc (NPL) and Sylvie Pierre (LNE-LNHB) for information exchange on particular aspects of the method. The author is also indebted to former colleagues of IRMM (CBNM) for their pioneering role in the development of the method and the construction of IRMM's DSA counters.

References

[1] Pommé S 2007 Methods for primary standardization of activity *Metrologia* **44** S17–26
[2] Broda R, Cassette P and Kossert K 2007 Radionuclide metrology using liquid scintillation counting *Metrologia* **44** S36–52
[3] Unterweger M P 2007 Primary radioactive gas standards (excluding radon) *Metrologia* **44** S79–81
[4] Sibbens G and Altzitzoglou T 2007 Preparation of radioactive sources for radionuclide metrology *Metrologia* **44** S71–8
[5] Bambynek W B 1967 Precise solid-angle counting *Standardization Radionuclides* (IAEA, Vienna SM-79/11) pp 373–83
[6] Spernol A and Denecke B 1971 Problems and improvements in low geometry alpha counting *Chemical Nuclear Data* ed M L Hurrell (London: The British Nuclear Energy Society) pp 199–203
[7] Mann W B, Rytz A and Spernol A 1988 Radioactivity measurements: principles and practice *Appl. Radiat. Isot.* **39** 717–937
[8] Denecke B, Eykens R, Pauwels J, Robouch P, Gilliam D M, Hodge P, Hutchinson J R M and Nico J S 1999 Characterization of actinide targets by low solid-angle alpha particle counting *Nucl. Instrum. Methods* A **438** 124–30
[9] Pommé S and Sibbens S 2008 Alpha-particle counting and spectrometry in a primary standardisation laboratory *Acta Chim. Slov*. **55** 111–9
[10] Robinson H P 1960 A new design for a high precision, high geometry α counter in: Metrology of radionuclides *Proc. of a Symp. organised by the IAEA* (*14–16 October 1959, Vienna*) 147–154
[11] Hutchinson J M R, Naas C R, Walker D H and Mann W B 1968 Backscattering of alpha particles from thick metal backings as a function of atomic weight *Int. J. Appl. Radiat. Isot.* **19** 517–22
[12] Flynn K F, Jaffey A H, Bentley W C and Essling A M 1972 Precision measurement of half-life and specific activity of ^{236}U *J. Inorg. Nucl. Chem.* **34** 1121–9
[13] García-Toraño E and Aceña Barrenechea M L 1989 Cámara de baja geometría para la medida absoluta de la actividad de muestras emisoras alfa *CIEMAT Technical Report* 626
[14] García-Toraño E, Durán Ramiro T, Burgos C and Begoña Ahedo M 2008 Defined solid-angle counter with variable geometry *Appl. Radiat. Isot.* **66** 881–5
[15] Blanchis P 1983 *Rapport CEA R*-5219
[16] Blanchis P 1984 Study of scattering in a low geometry alpha counter for high precision activity measurements *Nucl. Instrum. Methods* **223** 368–71
[17] Schötzig U, Schönfeld E and Janszen H 2000 Standardization and photon emission probabilities in the decay of ^{237}Np/^{233}Pa *Appl. Radiat. Isot.* **52** 883–9
[18] Picolo J L 1996 Absolute measurement of radon 222 activity *Nucl. Instrum. Methods A* **369** 452–7
[19] Dersch R 2004 Primary and secondary measurements of ^{222}Rn *Appl. Radiat. Isot.* **60** 387–90
[20] Spring P, Nedjadi Y, Bailat C, Triscone G and Bochud F 2006 Absolute activity measurement of radon gas at IRA-METAS *Nucl. Instrum. Methods* A **568** 752–59
[21] Gilliam DM and Yue AT 2014 Improvements in the characterization of actinide targets by low solid-angle counting *J. Radioanal. Chem.* **299** 1061–5
[22] Pommé S *et al* 2012 Measurement of the ^{225}Ac half-life *Appl. Radiat. Isot.* **70** 2608–14
[23] Papp Z 1997 Defined solid angle absolute β-counting for use in the radioanalysis of environmental samples *J. Radioanal. Nucl. Chem.* **222** 157–6
[24] Bambynek W, Lerch O and Spernol A 1966 Eine auf 1% genaue absolute zählung von x-strahlen geringer energie *Nucl. Instrum. Methods* **39** 104–8
[25] Huan L 1982 Edge penetration by radiation through a collimation system *Nucl. Instrum. Methods* **197** 411–6
[26] Owens A 1985 Calculation of the point source effective collimator aperture for collimated x-ray and γ–ray telescopes *Nucl. Instrum. Methods* A **239** 623–9
[27] Hosseini-Ashrafi M E and Spyrou N M 1992 Calculation of the average solid angle subtended by a photon-emitting source at a collimated detector and the contribution of collimator edge penetration *Appl. Radiat. Isot.* **43** 1449–60
[28] Burtt B P 1949 Absolute beta counting *Nucleonics* **5** 28–43
[29] Jaffey A H 1954 Solid angle subtended by a circular aperture at point and spread sources: formulas and some tables *Rev. Sci. Instrum.* **25** 349–54
[30] Segré E, Hanna G C, Deutsch M, Kofoed-Hansen O and Mc Millan E M 1959 Ed E Segré *Experimental Nuclear Physics* vol **3** (New York: Wiley) 437
[31] Zhang J, Chen X, Zhang C, Li G, Xu J and Sun G 2014 Development of a software package for solid-angle calculations using the Monte Carlo method *Nucl. Instrum. Methods A* **736** 40–5
[32] Pommé S 2007 Comments on 'A comparison of different analytical methods of determining the solid angle of a circular coaxial source-detector system' *Appl. Radiat. Isot.* **65** 1065–7
[33] Ruffle M P 1967 The geometrical efficiency of a parallel-disc source and detector system *Nucl. Instrum. Methods* **52** 354–6

[34] Ruby L and Rechen J B 1968 A simpler approach to the geometrical efficiency of a parallel-disk source and detector system *Nucl. Instrum. Methods* **58** 345–6
[35] Gotoh H and Yagi H 1971 Solid angle subtended by a rectangular slit *Nucl. Instrum. Methods* **96** 485–6
[36] Shelyuto V A 1989 Exact analytic results for the solid angle in systems with axial symmetry *J. Appl. Math. Phys.* **40** 608–14
[37] Zhihua W and Xinmiao W 1992 A new and simple approach to geometrical factor of a parallel disk source and detector system *J. Radioanal. Nucl. Chem. Lett.* **166** 211–17
[38] Ruby L 1994 Further comments on the geometrical efficiency of a parallel-disk source and detector system *Nucl. Instrum. Methods* A **337** 531–3
[39] Tryka S 1997 Angular distribution of the solid angle at a point subtended by a circular disk *Opt. Commun.* **137** 317–33
[40] Pommé S, Johansson L, Sibbens G and Denecke B 2003 An algorithm for the solid angle calculation applied in alpha-particle counting *Nucl. Instrum. Methods* **505** 286–9
[41] Sibbens G, Pommé S, Johansson L and Denecke B 2003 Tailoring solid angle calculations to the actual radioactivity distribution of planar sources *Nucl. Instrum. Methods* **505** 277–81
[42] Pommé S 2004 A complete series expansion of Ruby's solid-angle formula *Nucl. Instrum. Methods* A **531** 616–20
[43] Conway J T 2006 Generalizations of Ruby's formula for the geometric efficiency of a parallel-disk source and detector system *Nucl. Instrum. Methods* A **562** 146–53
[44] Conway J T 2007 Geometric efficiency for a parallel-surface source and detector system with at least one axisymmetric surface *Nucl. Instrum. Methods* A **583** 382–93
[45] Pommé S and Paepen J 2007 A series expansion of Conway's generalised solid-angle formulas *Nucl. Instrum. Methods* A **579** 272–4
[46] Pommé S 2007 The solid angle subtended by a circular detector for a linear source *Appl. Radiat. Isot.* **65** 724–7
[47] Conway J T 2008 Calculations for a disk source and a general detector using a radiation vector potential *Nucl. Instrum. Methods* A **589** 20–33
[48] Conway J T 2010 Analytical solution for the solid angle subtended at any point by an ellipse via a point source radiation vector potential *Nucl. Instrum. Methods* A **614** 17–27
[49] Conway J T 2010 Geometric efficiency for a circular detector and a linear source of arbitrary orientation and position *Nucl. Instrum. Methods* A **622** 555–66
[50] Conway J T 2011 Geometric efficiency for a circular detector and a ring source of arbitrary orientation and position *Nucl. Instrum. Methods A* **640** 99–109
[51] Martín Sánchez A, Bland C J and Fernández Timón A 2000 Computer simulation of backscattered alpha particles *Appl. Radiat. Isot.* **52** 341–6
[52] Fernández Timón A and Jurado Vargas M 2007 Dependence of α-particle backscattering on energy and source backing *Nucl. Instrum. Methods* A **580** 350–3
[53] Jaffey A H 1972 An effect of multiple scattering in a gas on the solid angle subtended by a circular aperture *Nucl. Instrum. Methods* A **103** 141–7
[54] NIST 1993 ASTAR webpage, http://www.nist.gov/pml/data/star/, based on ICRU Report 49, *Stopping Powers and Ranges for Protons and Alpha Particles* (1993)
[55] Pommé S, Wagemans C, Verhaegen F, Van Den Durpel L, Van Gils J and Barthelemy R 1995 A double ΔE-E detection set-up for ternary fission *Nucl. Instrum. Methods* A **359** 587–95